

Simultaneous Birefringence and Absorption Mapping in Large-Size Sapphire Substrates for Gravitational-Wave Interferometry

Simon Zeidler (✉ s.zeidler@rikkyo.ac.jp)

Rikkyo University

Pengbo Li

National Astronomical Observatory of Japan (NAOJ)

Marc Eisenmann

National Astronomical Observatory of Japan (NAOJ)

Marco Bazzan

Università di Padova

Matteo Leonardi

National Astronomical Observatory of Japan (NAOJ)

Article

Keywords:

Posted Date: April 20th, 2022

DOI: <https://doi.org/10.21203/rs.3.rs-1563039/v1>

License:  This work is licensed under a Creative Commons Attribution 4.0 International License.

[Read Full License](#)

Simultaneous Birefringence and Absorption Mapping in Large-Size Sapphire Substrates for Gravitational-Wave Interferometry

Simon Zeidler^{1,3,+,\dagger}, Pengbo Li^{1,2}, Marc Eisenmann¹, Marco Bazzan⁴, and Matteo Leonardi^{1,*}

¹National Astronomical Observatory of Japan (NAOJ), Gravitational Wave Science Project, Tokyo, 181-8588, Japan

²School of Physics and Technology, Wuhan University, Wuhan, 430072, China

³Rikkyo University, Department of Physics, Nishiikebukuro 3-34-1, Toshima-City, Tokyo, 171-8501, Japan

⁴Dipartimento di Fisica e Astronomia, Università di Padova, Padua 35131, Italy

^{\dagger}s.zeidler@rikkyo.ac.jp

*matteo.leonardi@nao.ac.jp

+Corresponding Author

ABSTRACT

In high-sensitive laser interferometers, such as the gravitational-wave detector KAGRA, ultra-high quality mirrors are essential. In the case of KAGRA, where cavity-mirrors are cooled down to 20K, we are using large-size Sapphire crystals as the substrate for the main mirrors to achieve both a good optical quality (i.e., low absorption and uniform refractive index) and optimized thermal behavior under cryogenic temperatures. In order to characterize refractive-index inhomogeneities of large-size uniaxial samples such as the KAGRA Sapphire test-masses, we developed a dedicated setup, allowing to resolve birefringence changes with a sensitivity in the order of $\Delta n \approx 10^{-10}$ and a spatial resolution of $0.3 \times 0.3 \text{ mm}^2$. In this paper, we will further show how we could draw information of internal stress distributions from the measured birefringence and present for the first time measurements on a KAGRA-sized Sapphire substrate which has been characterized in terms of absorption already in an earlier work. Both birefringence inhomogeneities and absorption distributions will be compared and correlations discussed.

Introduction

Sapphire has become an important material in many optical applications. Not only in industry but also in optical science, Sapphire is essential for utilizing instruments and measurements due to its robustness and versatility. In KAGRA^{1,2}, the Japanese second-generation gravitational-wave detector, Sapphire plays a key-role as well. In contrast to the LIGO detectors³ in the USA and the Virgo detector⁴ in Italy, KAGRA uses cryogenic mirrors as test-masses inside the laser-interferometer. Under such conditions, Silica (amorphous SiO_2), which is the most widely used mirror-substrate material, would not be beneficial as it shows increased internal friction and insufficient thermal conductivity⁵ which would in any case harm the detector's targeted sensitivity due to thermal noise. In order to profit from the cryogenic condition, a material is needed which features an increased thermal conductivity at low temperatures and having optical as well as mechanical properties sufficient for a mirror substrate. Sapphire in principle possesses all those characteristics and is therefore one of the materials of election for the next generation of cryogenic gravitational-wave detectors⁶.

Sapphire is a variety of crystalline Al_2O_3 which crystallizes in a trigonal crystal system. The oxygen anions are arranged in a (slightly distorted) hexagonal close-packing in which the aluminum cations occupy two thirds of the octahedral interstices^{7,8}. In a hexagonal unit-cell, we can differentiate between a distinct axis along the hexagon's height (c-axis) and 3 axes perpendicular to the c-axis representing the 3 symmetry-directions of a hexagon's barrel. This lattice structure basically leads to a non-isotropic behavior of Sapphire crystals when it interacts with light. The refractive index is different for the electric field polarized parallel (extraordinary) or perpendicular (ordinary) to the c-axis, hence leading to birefringence.

Nowadays, the growing mechanism of large Sapphire single-crystals with diameters up to 300mm are quite sophisticated and samples of decent optical quality can be manufactured. The most common techniques to produce large Sapphire crystals are the Czochralski and the Kyropoulos methods where a single-crystal is slowly being grown from a melt using a condensation seed⁸. Nevertheless, impurities and imperfections within the lattice structure give rise to absorption centers in Sapphire crystals which (from the standpoint of gravitational-wave detectors) are still a limiting factor when compared to manufactured Silica, especially for large-size samples. Particularly Fe, Ni, and Si but also Cr and Ti are common impurities in alumina⁸ whereby

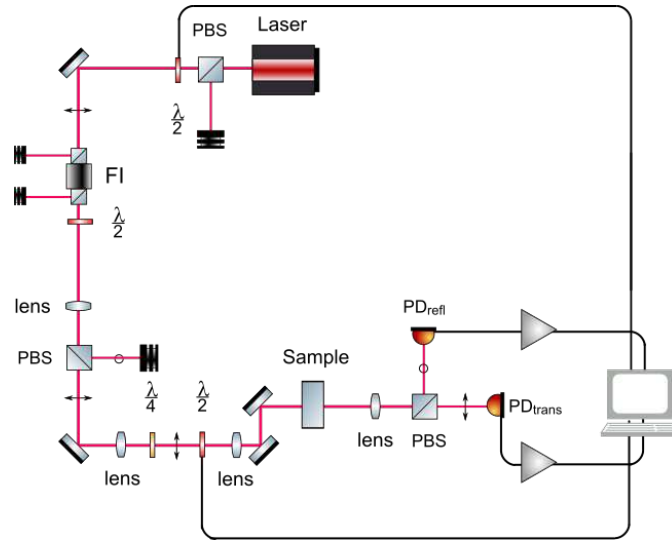


Figure 1. Left: Layout of the experimental setup to measure the birefringence distribution of a sample. The sample itself is placed on a movable stage (not included in the figure).

their presence is correlated with vacancies in the lattice. When present, Fe, Ni, and Cr ions can substitute Al cation sites^{8,9} but, due to their larger size, will distort the local lattice structure. In addition, residual thermal induced stress during the manufacturing process may remain inside the lattice and lead to density anisotropy or to the formation of dislocation networks which in turn may affect the refractive index as well. For smaller sized Sapphire crystals these issues may be not so severe as the manufacturer is able to carve from the as-grown boule those regions which are of highest quality. However, for larger Sapphire crystals, having sizes significantly close to the size of the boule, this is not possible and can cause issues especially for applications that require highly homogeneous optical properties, as in the case of gravitational-wave interferometry¹⁰.

In this paper, we will present the results of our efforts to characterize birefringence inhomogeneities for large Sapphire crystals and correlate them with spatially resolved absorption measurements. In Section 2 of this paper (after the introduction), the main focus will be to describe the features of our measuring system before we turn to a brief overview on the mathematical background of birefringence measurements and the subsequent conclusions on internal stress from the viewpoint of our system. In section 3 then, we are presenting results from measurements on two Sapphire samples, highlighted by those from a KAGRA-sized (\varnothing : 220mm; thickness: 150mm) Sapphire bulk. The obtained birefringence map is compared to linear absorption maps obtained using the setup described in Marchiò et al. (2021)¹¹, in order to search for a possible correlation between the stress distribution in the sample and the presence of absorption centers. In section 4, we will discuss our results and present annealing as a possible measure to reduce birefringence effects.

Experimental Setup

Modified PCI

At NAOJ, we have established a so-called Photothermal Common-Path Interferometer (PCI)¹² in order to produce spatially resolved maps of the absorption coefficient for various transparent materials¹¹. We modified the system particularly to characterize large mirror substrates that are of concern for KAGRA (cylindrical, 220mm diameter and 150mm thickness) but also optics below that size can easily be characterized. We modified the setup slightly to enable measuring birefringence maps by analyzing the polarization state of the exiting beam keeping the possibility to hold and move KAGRA-sized substrates. We configured the main laser of the PCI (OXIDE LS0100-F1) so to control its power and polarization, and added an optical isolation system (Faraday isolator) so to protect the laser from back-reflections and to clean the polarization of the incident beam. A remotely controlled half-wave-plate (HWP) combined with a polarizing beam-splitter (PBS) in front of the Faraday isolator serves as a quite effective power-control (dynamic range: $\sim 1:9000$). In addition to the isolator, we placed a quarter-wave-plate (QWP) and a HWP (also remotely controllable) into the beam-path which are further cleaning the polarization so to reduce circular polarized portions to a minimum and have a linearly polarized beam. By setting another PBS and two photodetectors (PD) after the sample, we could measure the power of the S and P components of the transmitted beam and compute the power-ratio $P_{s,p}/(P_s + P_p)$ down to 10^{-5} for each polarization. In order to increase the signal-to-noise ratio, we are chopping the laser at 375Hz and connect each PD with a lock-in amplifier to decouple the signal with the chopper frequency. In Fig.1 the

Our device is basically a *plane-polariscope* or *linear-polariscope*^{13,16}: we inject light with a known polarization into a sample and analyze the transmitted polarization relative to it (see also Fig.2). However, in usual plane-polariscopes, one would adjust the input polarizer perpendicular to the output polarizer (analyzer) and rotate the sample¹⁶ so that a calculation of the birefringence is directly possible via the measurements. Since the polariscope in our case is different as the incident polarization is rotated and we use a PBS instead of an analyzer, we will show in this section how the information may be retrieved nevertheless.

As for the definition of a proper reference frame, we assume our probe beam is propagating through the sample in direction Z and the c-axis of the Sapphire sample is parallel to that direction. Thus, we set the (unperturbed) dielectric tensor ε as

$$\varepsilon = \begin{pmatrix} \varepsilon_o & 0 & 0 \\ 0 & \varepsilon_o & 0 \\ 0 & 0 & \varepsilon_e \end{pmatrix}, \quad (1)$$

where $\varepsilon_o = 1/n_o$, $\varepsilon_e = 1/n_e$ (see also Fig.2 for a description of the reference frames and denominations). In this condition, the index-ellipsoid (indicatrix) seen by the input beam has a circular section and the sample is optically isotropic for the beam propagating along the Z direction. Any stress perturbation induces a modification of the sample's birefringence via the photo-elastic effect. In this case, the indicatrix will be deformed by a quantity Δn and tilted by an angle θ as shown in Fig.2. Our goal is thus to estimate those two quantities with our measurements.

In order to solve the problem for θ and Δn , we are using two different input polarization angles. Defining the input polarization angle as γ (measured as off-angle from the vertical direction in our global coordinate system), we consider two different cases: $\gamma = 0$ (S-polarized input beam) and $\gamma \neq 0$. Considering the first case, let I_s^0 and I_p^0 be the intensities of the two output beams exiting from the final PBS, it can be shown that^{13,17}:

$$\frac{I_s^0}{I_p^0} = \frac{1}{\sin(\delta n)^2 \sin(2\theta)^2} - 1, \quad (2)$$

with $\delta n = \pi/\lambda \cdot d \cdot \Delta n$ where Δn is the stress-induced birefringence and λ the wavelength of the laser. Taking now the intensity of the S-polarized exiting beam for the case $\gamma \neq 0$, we find after a careful calculation of the transmitted electric field in phasor notation:

$$I_s = I_0 \cdot \left\{ \cos(\gamma)^2 + \sin(\delta n)^2 \left[\frac{1}{2} \sin(2\gamma) \sin(4\theta) - \sin(2\theta)^2 \cos(2\gamma) \right] \right\}. \quad (3)$$

Solving Eq.(2) for $\sin(\delta n)$ and inserting the result into Eq.(3), we end with an expression for θ based purely on the measured intensities for the two input polarization cases

$$\theta = 0.5 \cdot \arctan \left\{ \frac{\tilde{A} \sin(2\gamma)}{\frac{I_s}{I_0} - \cos(\gamma)^2 + \tilde{A} \cos(2\gamma)} \right\}, \quad (4)$$

where $\tilde{A} = I_p^0/(I_s^0 + I_p^0) = I_p^0/I_0^0$, is the ratio of the P polarized beam intensity after the PBS to the total transmitted intensity before the PBS for $\gamma = 0$. On the other side, we find for Δn :

$$|\Delta n| = \frac{\lambda}{d\pi} \arcsin \sqrt{\frac{I_p^0}{I_p^0 + I_s^0} \cdot \frac{1}{\sin(2\theta)^2}}. \quad (5)$$

It should be noted that Iwaki and Koizumi (1989)¹⁷ come to similar conclusions in spite of the fact that they were using cubic silicon as sample. This can be understood due to the fact that we are basically measuring the projection of the indicatrix on the ordinary plane, where we expect only stress-induced birefringence effects and otherwise optical isotropy, similarly to cubic crystals.

Stress applied to the sample, which is usually described in form of a tensor s , affects the indicatrix of the anisotropic optical system. The (material specific) coefficients which determine the change of the indicatrix are in turn given by a fourth-rank

p_{11}	p_{12}	p_{13}	p_{14}	p_{31}	p_{33}	p_{41}	p_{44}
-0.037	1.396	2.163	0.014	0.3	-0.539	0.225	-2.916

Table 1. Components of the opto-elastic tensor for Sapphire. Given in units of 10^{-3} GPa^{-1} .

elasto-optic tensor p ¹⁸. Using the Voigt's notation and taking into account the symmetries in a trigonal system, p for Sapphire writes as¹⁹:

$$p = \begin{pmatrix} p_{11} & p_{12} & p_{13} & p_{14} & 0 & 0 \\ p_{12} & p_{11} & p_{13} & -p_{14} & 0 & 0 \\ p_{31} & p_{31} & p_{33} & 0 & 0 & 0 \\ p_{41} & -p_{41} & 0 & p_{44} & 0 & 0 \\ 0 & 0 & 0 & 0 & p_{44} & 2p_{41} \\ 0 & 0 & 0 & 0 & p_{14} & p_{11} - p_{12} \end{pmatrix} \quad (6)$$

The components of p are known in case of Sapphire and given in table 1. Under stress, the indicatrix becomes tilted and deformed. In the following we will indicate with Δn the indicatrix deformation in the plane perpendicular to the beam propagation direction (i.e., perpendicular to the c -axis), which is equal to the stress-induced birefringence, and θ the angle formed by the indicatrix' principal axis with respect to Y (see also Fog.2). By using the model of a deformed ellipsoid which is projected on a plane, the following relation can be obtained:

$$\begin{aligned} (s_1 - s_2) + 2s_4 \cdot \frac{p_{14}}{p_{11} - p_{12}} &= \frac{2|\Delta n|}{n_o^3(p_{11} - p_{12})} \cdot \cos(2\theta) \\ s_6 + s_5 \cdot \frac{p_{14}}{p_{11} - p_{12}} &= \frac{4|\Delta n|}{n_o^3(p_{11} - p_{12})} \cdot \sin(2\theta), \end{aligned} \quad (7)$$

where we have used an eigenvalue decomposition of the projected indicatrix and the reasonable assumption that the birefringence effect is weak ($\Delta n \ll n_o, n_e$). Using our method, we are able to measure, point by point, the characteristics of the optical indicatrix Δn and θ . From those data, however, we have not enough information to solve for each component of the stress tensor independently. We will thus write

$$\begin{aligned} (s_1 - s_2) + 2s_4 \cdot \frac{p_{14}}{p_{11} - p_{12}} &= \hat{s}_0 \\ s_6 + s_5 \cdot \frac{p_{14}}{p_{11} - p_{12}} &= \hat{s}_1 \end{aligned} \quad (8)$$

and refer to \hat{s}_0 and \hat{s}_1 as projected stress influence.

Results

Selection of Samples and Absorption Characterization

Basically, we had four types of samples available for our measurements: 3×1 " diameter, 2×2 " diameter, 2×100 mm diameter, and 4×220 mm diameter Sapphire single-crystals (cylindrical cut with the c -axis perpendicular to the two main surfaces). The 1" and 2" samples have a thickness of 10 mm, while both 100 mm samples have a thickness of 60 mm and the 220 mm samples a thickness of 150 mm. All samples are from the same manufacturer but from different boules.

Before performing the birefringence measurement, we characterized each sample in terms of the absorption coefficient distribution (we refer here to the linear absorption coefficient) using the Photoinduced Common-Path Interferometry (PCI) method described in Marchiò et al. (2021)¹¹. As the PCI setup and the birefringence setup are built on the same optical table and share the laser source and the same sample positioning system, the two maps can be conveniently superimposed in order to evidence any correlation between the linear absorption and the birefringence maps. For this paper, we decided to present the results of a 100 mm and a 220 mm diameter sample which is the same presented already in an earlier paper by Marchiò et al. (2021)¹¹. A list of their basic parameter can be found in Table 2 together with their mean absorption coefficient and their denomination (T1 and S7), which will be also used in this paper.

In Fig. 3 the absorption coefficient distribution of those two samples are presented. To be safe, we limited map-taking to a region around the center axis of each sample, keeping usually a margin of $\gtrsim 1/3$ of a sample diameter to the outer edges. Please note that the map for T1 represents the absorption distribution in the center of that sample (measured at $Z = 64, 24$ mm

sample	size	absorption coefficient (mean) [ppm/cm]	comment
T1	\varnothing : 100mm d : 60mm	23.30 ± 4.35	annealing scheduled
S7	\varnothing : 220mm d : 150mm	61.56 ± 17.11	

Table 2. Overview of the basic properties for the two presented samples. The respective denomination is given in the first column, while the sizes are given in the second. Note that the samples are cylindrical (d refers to the thickness). For T1, we have plans for annealing in the future.

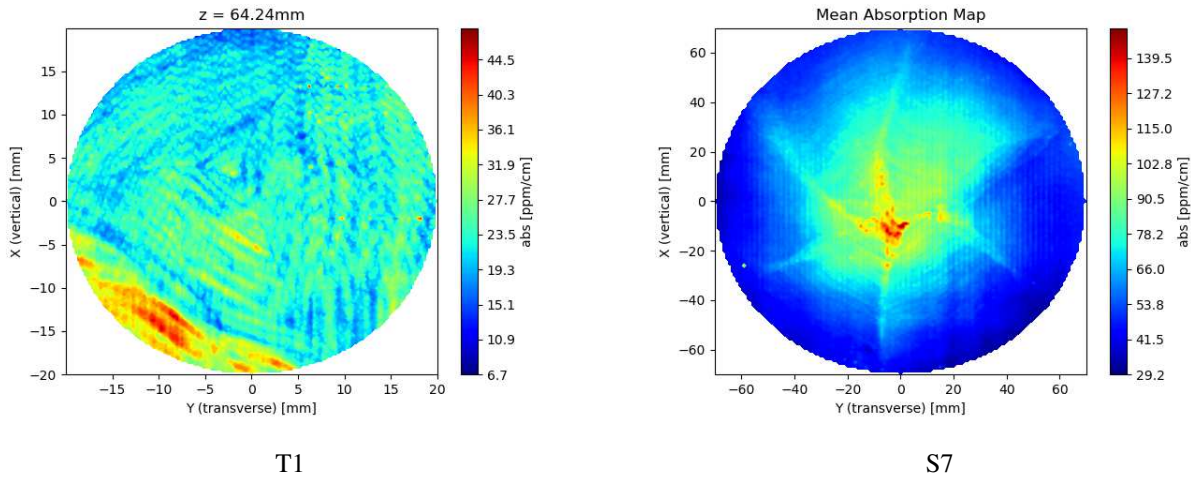


Figure 3. Overview of the absorption coefficient distribution for the T1 and the S7 sample.

of the PCI system), while the map for S7 represents the mean absorption throughout the entire sample (calculated by averaging 7 single maps).

As can be seen, there is a three-folded structure visible in case of T1 with absorption fringes (local excesses in absorption) oriented accordingly, forming a pattern of equable quasi-triangles. The fringes have a distance of roughly $1 \sim 4$ mm to each other and are present not only in the center right-section but throughout the whole sample. In comparison, S7 shows a star-like pattern with a clear absorption peak in the center. Also here fringes are visible with orientations according to each sub-segment. The distance between the fringes appears to be of the same order as for T1. Both the three/six-fold symmetry and the fringes are probably remnants from the manufacturing process (“growth striations”)^{8,11}. Especially the symmetries reflect hereby the symmetries of the crystal-structure of Sapphire. The maps in Fig. 3 have been taken with a resolution of 0.5×0.5 mm and 1×1 mm, respectively. Taking higher resolution measurements resolved even finer structures. But since they are out of the scope of this paper, we will not present them here. The interested reader is guided to the work by Marchiò et al.¹¹ for further study.

Birefringence Maps

In Fig. 4, maps of the two samples are presented showing the distribution of the birefringence effect in terms of a “polarization angle” ξ which we defined as a supporting parameter (see also Fig.2) and is given as

$$\xi = \arctan \left(\sqrt{\frac{P_s}{P_p}} \right), \quad (9)$$

with P_s and P_p being the measured power of the transmitted S- and P- polarized parts of the beam. The input polarization was S ($\gamma = 0^\circ$), while the orientation of the samples remains the same as for Fig. 3. Differently from the usual absorption map, which is a section at a given sample depth obtained thanks to the three-dimensional spatial resolution of the PCI setup, the information from the polarization angle (and birefringence) maps is naturally averaged along the whole sample thickness. For

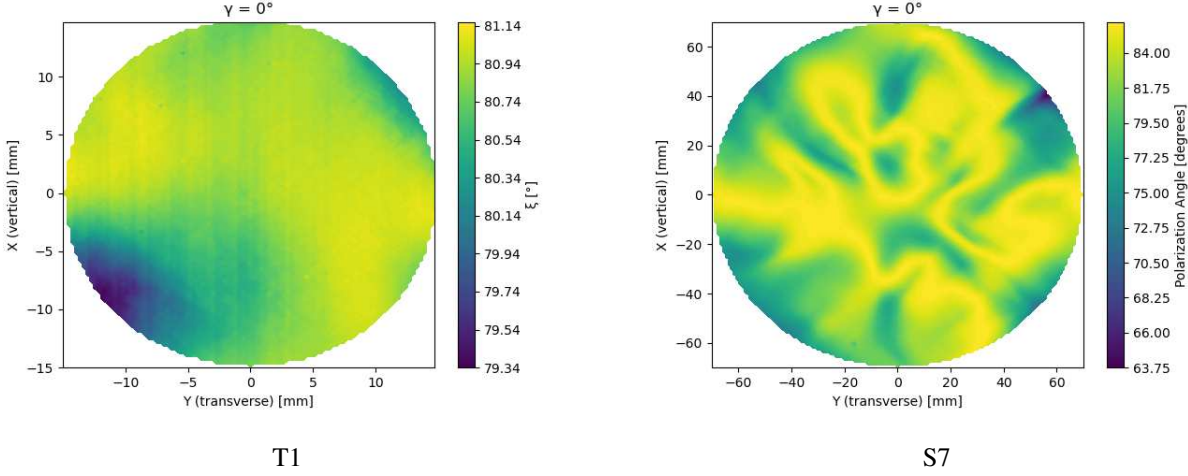


Figure 4. Overview of the birefringence effect for the T1 and S7 sample in terms of the polarization angle ξ (see text).

that reason we have created an averaged absorption map of S7 to include absorption distributions along Z as well. However, a direct comparison still remains to be on a qualitative level since only a finite number of sections could be used for the averaging. Anyway, the main structures in absorption appear to be relatively invariant along Z (T1 as well as S7¹¹). Thus, a direct comparison with birefringence maps is indeed reasonable. In fact, when inspecting S7 in particular and comparing the two absorption and polarization angle maps, we can spot a correlation between absorption and birefringence features. Fringes or similar patterns, however, cannot be observed. Please note, that the vertical stripes which are visible especially for T1 (but also in absorption for S7) are from the device due to tiny fluctuations in the polarization of the incoming beam and are not features of the samples.

In case of T1, we see a rather homogeneous distribution of ξ . There is a drop towards the bottom left (negative X and Y) in an area where we also see an increase in absorption. The same seems to be true for the bottom-right (negative X and positive Y) and upper-right sections. For S7, on the other side, the distribution is inhomogeneous, loosely following the symmetric structures visible in absorption, as stated above. But there are also features in the polarization angle maps which doesn't seem to have an equivalent in absorption. For example, we see several "sinks" in ξ (e.g., center-top or top-right) and meandering "lines" of high ξ values which are unique features of the polarization angle map.

The given distribution in terms of ξ is a direct evidence that birefringence inhomogeneities introduce a measurable depolarization of the optical beam and shows already the basic problematic of using Sapphire substrates in gravitational waves detectors like KAGRA. To better investigate the birefringence distribution in our sample, we have taken several maps as the one shown in Fig. 4 with varying input polarization γ and extract the information of Δn and θ according to Eqs.(2) to (4). In the following, we will concentrate on S7 since its absorption maps have been reported already¹¹.

γ has been varied from 0° (S-polarized) to 75° in steps of 15° (for more accurate values, see, e.g., the legend in Fig.6). From the resulting maps, we calculated the distribution of $|\Delta n|$ and θ for each input polarization against the $\gamma = 0^\circ$ map, resulting in 5 independent pairs of $|\Delta n|$ and θ distribution maps. In theory, the choice of γ does not affect the result of the measurement. Therefore, maps taken at different γ should coincide. Variations in the obtained values can be thus taken as an estimation of the method's reproducibility. The mean distribution for both parameters has been calculated from these maps and is plotted in Fig.5 in an overlapping graph. While $|\Delta n|$ is given in form of a color-map, θ is put atop as a distribution of streamlines giving the orientation of the axis along which an electric field experiences n_1 (refer to Fig.2), whereby the vector $v = (Y_v, X_v)$ forming each streamline is defined with $Y_v = \sin(\theta)$ and $X_v = \cos(\theta)$. The structures which appeared in Fig.4 are defined by the $|\Delta n|$ distribution, which is a measure for the magnitude of internal stress according to Eq.(7). As can be seen, the meandering pattern turns out to be the minimum in $|\Delta n|$ which marks at the same time a border between areas of basically two different θ value concentrations: one at small ($5 \sim 10^\circ$) and one at large values ($80 \sim 85^\circ$). This may be due to the fact that we are not able to distinguish between positive and negative Δn since either will lead to the same resulting ξ .

At this point, we also mention some statistics regarding $|\Delta n|$ and θ from each input polarization measurement. In Fig.6, the probability density histograms of these parameters for all 5 input polarization maps is presented. As mentioned above, the maps should be physically identical, independent of γ , and so should also the histograms. Despite of minor discrepancies this seems to be the case for both Δn and θ . At the same time, it can be observed that the histograms do not cover any zero value. The minimum in Δn lies at $\sim 1.5 \cdot 10^{-7}$ where in the histogram we recognize a peak at this position. Taking into account the noise

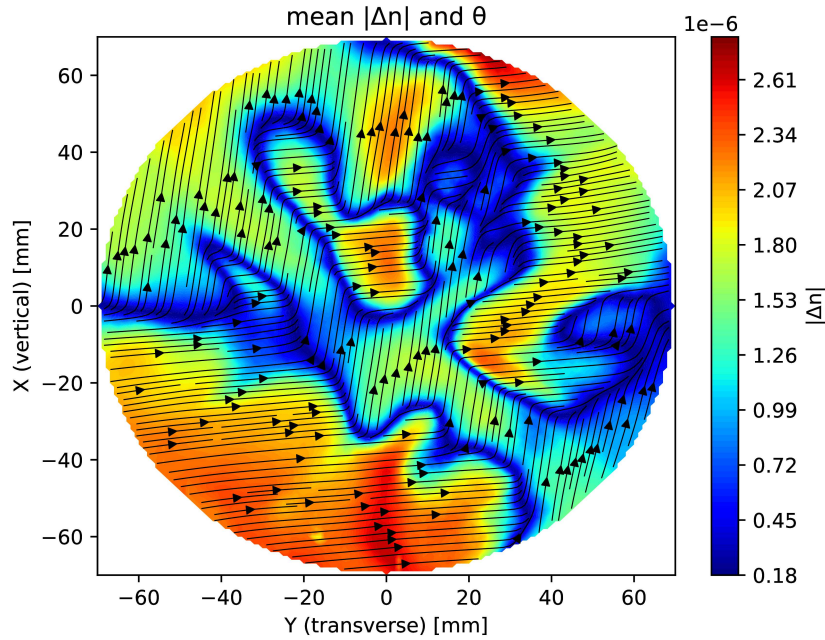


Figure 5. Combined plots of both mean $|\Delta n|$ and θ from all measured maps of S7 calculated according to Eqs.(4) and (5). θ is given as streamlines pointing to the direction of an internal stress vector, while $|\Delta n|$ is represented by an underlying color-map.

floor, the photodiodes should enable us to resolve the birefringence down to 10^{-8} . Therefore our result seems to indicate that a non-zero constant birefringence background is present over all the examined area. This can be attributed to a small miscut of the c axis with respect to the major surfaces normal. A c-axis misalignment for example of the order 0.2° would have the same effect as a birefringence of $\sim 1.5 \cdot 10^{-7}$ for small θ values (see also the discussion section).

The histogram for θ reflects our main observation from Fig.5. We see two peaks at $5 \sim 10^\circ$ and at $80 \sim 85^\circ$. Since in our method the θ values are restricted to be positive, due to the arctangent in Eq.(4), we may interpret this as an angle-wrapping effect in the sense that we actually have only one concentration at around 0 (or $\pi/2$), given θ is permitted to become negative as well. It is nevertheless remarkable that there are no θ values at 0° (or 90°) and that both distributions resemble in shape the χ^2 -distribution.

Internal Stress Distribution

In Fig.7, we can see a color map of the two effective stress parameters \hat{s}_0 and \hat{s}_1 . The maximum absolute value in both distributions does not exceed 0.7MPa. The structures visible resemble the distribution of $|\Delta n|$, as expected, while the θ distribution has only a marginal influence due its compact concentration at either around $5^\circ \sim 10^\circ$ or $80^\circ \sim 85^\circ$. Only the sign of \hat{s}_0 is being affected due to its $\cos(2\theta)$ dependence (see Eq.(7)). In both maps we recognize again the meandering pattern as the minimum magnitude along which \hat{s}_0 changes its sign. Inspecting Eq.(7), that change may be attributed to either a negative s_4 (shear-stress in Y - Z) which becomes larger in magnitude than $(s_1 - s_2)$ (normal-stress difference in X - Y) or vice versa. However, since the presented stress-maps are just projections of the actual stress-tensor, we cannot state anything beyond the given mathematical relations.

Discussion

Taking S7 as a prime example, we have shown the effect of birefringence in large Sapphire substrates on the polarization of a transmitted laser beam. From the calculated birefringence orientation (θ) and its strength ($|\Delta n|$), we could conclude about the projected stress influences \hat{s}_0 and \hat{s}_1 which are both in the range of a few hundred thousand Pascal. We could show that the (thickness averaged) stress tensor ellipsoid is oriented so that its normal directions remain more or less constant along the sample volume.

The birefringence appears to be related to the absorption coefficient distribution, which in turn may have its origin in the manufacturing process^{8,11,20} (this has been pointed out also by a previous research using transmitted wavefront error maps²¹).

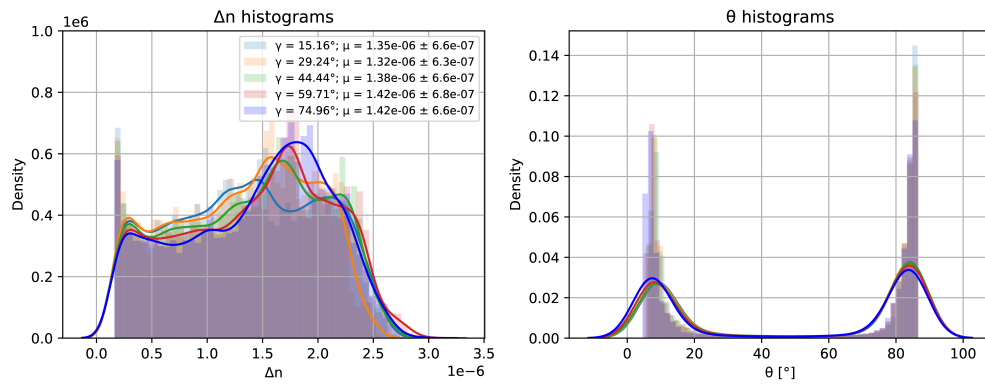


Figure 6. Histograms of both $|\Delta n|$ and θ parameter distributions for all three input polarization angles (against $\gamma = 0^\circ$) and the calculated mean distribution for both possible solutions. The histograms are plotted in terms of their probability density together with an estimated probability density function. The mean value μ (\pm standard deviation) of $|\Delta n|$ is given in the legends.

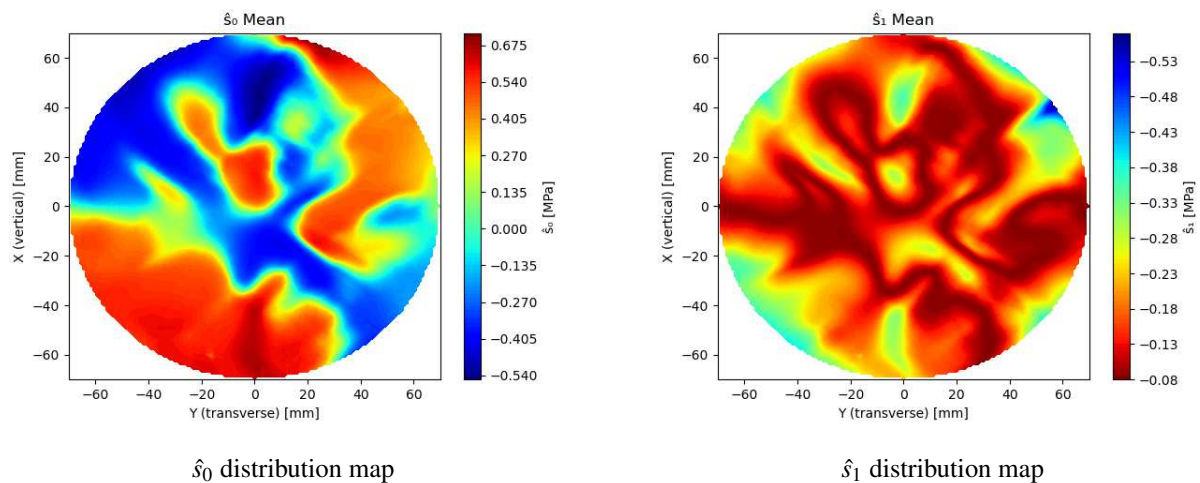


Figure 7. Mean stress parameter distribution maps for the S7 sample calculated from five different input polarization maps against the $\gamma = 0^\circ$ polarization (see text for further details).

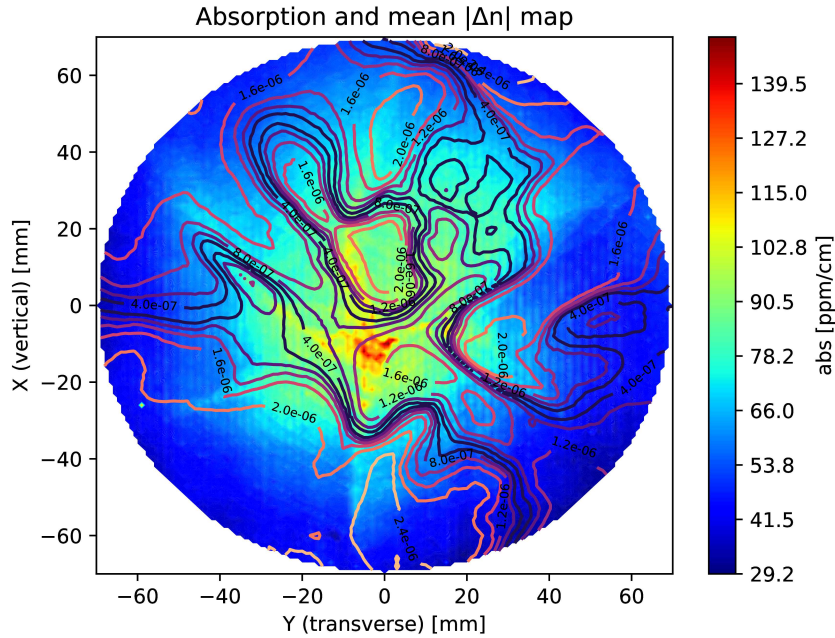


Figure 8. Overlay plot of the mean-absorption map shown in Fig.3 and the mean Δn distribution. The latter is given as a contour plot with the respective values given inside the figure.

In Fig.8, an overlay plot of both the absorption coefficient as given in Fig.3 and $|\Delta n|$ as given in Fig.5 is presented. In case of the most prominent features in $|\Delta n|$ we see that they lie either in between or close to the radial absorption lines forming the aforementioned star-like structure. Exceptions from this correlation are only present at the edges of the measured area. It has been pointed out already that the star-like structure visible in the absorption map actually marks the edges of growth planes¹¹ which are known to attract impurities such as transition elements or vacancies. Point defects, on the other side, may act as source of compositional stress. This finding is also supported by the maps shown for sample T1, which present a rather homogeneous distribution of both absorption coefficient and ξ -angle. In regions where absorption increases, the ξ -angle indeed changes as well. From the results presented for S7, we see increased birefringence also in regions where no absorption centers are visible (e.g., in the bottom area). This may be a hint for the existence of either impurities in those regions which do not act as absorption centers at $\lambda = 1064$ nm or remaining stress induced by thermal gradients from manufacturing. Unfortunately the birefringence data are not sufficient to fully reconstruct the whole stress tensor, and our data must be interpreted only in terms of the effective stresses. At the moment it appears difficult to relate quantitatively the stress field with the impurity distribution and it would be a task for future investigation.

We could show that there are apparently two preferred directions of the birefringence as θ is accumulating at values $5^\circ \sim 10^\circ$ and $80^\circ \sim 85^\circ$, leading to a change of sign in \hat{s}_0 whenever θ changes from one direction to the other. The reason for these preferred directions, however, is yet unknown. Given the fact that positive ($n_2 > n_1$) and negative ($n_2 < n_1$) Δn are likely to exist throughout the whole measured area, it may be that the two θ distributions are hinting to an inversion in sign of Δn . This inversion would affect also the stress-tensor but is only speculative in the moment and would be a matter of later measurements.

If we follow the argument that local stress due to vacancies, impurities or other imperfections are the origin of crystal-structure (and hence birefringence) inhomogeneities, then sample annealing could be a possible way to reduce it to a certain extent. In fact, oxygen vacancies, diffusive impurities and defect clusters may be redistributed, leading to a more homogeneous defect concentration and thus smoothing out the stress fields⁸. On the other hand, impurities in oxides are optically active at wavelengths in the ultra-violet and visible range^{22,23} and in most cases, we can clearly identify them in UV-VIS spectra from Sapphire samples smaller than the one presented in this paper as a relatively strong and broad absorption band at around 250 ~ 260 nm wavelength, which is a clear indication of F+ type color centers^{24,25}. At longer wavelengths, we were able to identify several other absorption bands (especially at around 350, 400 and 450 nm). In particular a band at 400 nm is probably due to Cr^{3+} ions²⁴. Transition-metal impurities are substitutional defects which are strongly bond within the oxygen cage which constitute the Sapphire structure. Those defects are difficult to be removed by annealing. However thermal treatments

can be used at least to modify their oxidation state²⁵, which eventually will remove at least their contribution to absorption.

In order to investigate the possibilities to reduce birefringence that come with annealing, we have given a 2" sample and T1 to the "Institut Lumière Matière" (ILM) in France where a furnace capable of sustaining temperatures above 1600°C over several days and working under different atmospheres exists. We are currently analyzing the preliminary results which we got from ILM. A forthcoming paper on the annealing of Sapphire and its influence on birefringence is planned.

Conclusion

We developed a system which is able to perform polarization measurements on large-size sapphire samples to be used as test masses for gravitational wave detectors. Using this system we were able to obtain position-resolved birefringence data and interpret them in terms of residual stress fields present in the sample. The setup is integrated within the PCI system at the TAMA laboratory in NAOJ (Tokyo) which results in a unique compilation of having both absorption and birefringence distributions of a large sample without changing its orientation.

We could show for samples T1 and S7 that there is a correlation between the distribution of the absorption coefficient and the birefringence. Moreover, we have presented a method how to extract information on the internal stress distribution from the birefringence measurements and analyzed them for a specific sample. Due to the results, we can say that the compositional absorption inhomogeneities are an important factor for increased internal stress and thus the birefringence structures which we observed. For the first time, we were able to analyze these structures on Sapphire samples having sizes above 200mm diameter and thicknesses of 150mm, the size of a KAGRA test mass. Although the actual effect of the birefringence inhomogeneities may be negligible for thinner samples, our work proofs the necessity in gravitational-wave detector science to be able to measure very thick samples since the cumulative effect increases linearly with the thickness and may be underestimated by concentrating on small samples only.

In this regard, we would like to mention that this work shall be just a first paper in a series concerning the birefringence in Sapphire. Currently, we are upgrading the modified PCI further to become a *circular-polariscope*^{13,16} with which we can reduce the amount of maps necessary for a birefringence calculation.

References

1. Akutsu, T. *et al.* Kagra: 2.5 generation interferometric gravitational wave detector. *Nat. Astron.* **3**, 35, DOI: [10.1038/s41550-018-0658-y](https://doi.org/10.1038/s41550-018-0658-y) (2019). [1811.08079v1](https://arxiv.org/abs/1811.08079v1).
2. Akutsu, T. *et al.* Overview of kagra: Detector design and construction history. *Prog. Theor. Exp. Phys.* **2021**, DOI: [10.1093/ptep/ptaa125](https://doi.org/10.1093/ptep/ptaa125) (2020). 05A101, <https://academic.oup.com/ptep/article-pdf/2021/5/05A101/37974994/ptaa125.pdf>.
3. Aasi, J. *et al.* Advanced LIGO. *Class. Quantum Gravity* **32**, 074001, DOI: [10.1088/0264-9381/32/7/074001](https://doi.org/10.1088/0264-9381/32/7/074001) (2015).
4. Acernese, F. *et al.* Advanced virgo: a second-generation interferometric gravitational wave detector. *Class. Quantum Gravity* **32** (2015).
5. Courtens, E., Foret, M., Ruffle, B. & Vacher, R. Elasticity and anelasticity of oxide glasses. *Phys. Chem. Glasses: Eur. J. Glass Sci. Technol. B* **48**, 9–18 (2007).
6. Cahill, D. G. & Pohl, R. O. Lattice vibrations and heat transport in crystals and glasses. *Ann. Rev. Phys. Chem.* **39**, 93–121 (1988).
7. Zeidler, S., Posch, T. & Mutschke, H. Optical constants of refractory oxides at high temperatures - the mid-infrared properties of corundum, spinel and α -quartz. *Astron. & Astrophys.* **553**, A81 (2013).
8. Dobrovinskaya, E. R., Lytvynov, L. A. & Valerian, P. *Sapphire - Material, Manufacturing, Applications* (Springer, 2009).
9. Gaudry, E. *et al.* Structural relaxations around ti, cr and fe impurities in α -al₂o₃ probed by x-ray absorption near-edge structure combined with first-principles calculations. *J. Physics: Condens. Matter* **17**, 5467 (2005).
10. Abe, H. *et al.* Performance of the kagra detector during the first joint observation with geo 600 (o3gk). *arXiv preprint arXiv:2203.07011* (2022).
11. Marchiò, M., Leonardi, M., Bazzan, M. & Flaminio, R. 3d characterization of low optical absorption structures in large crystalline sapphire substrates for gravitational wave detectors. *Sci. Reports* **11**, 1–8 (2021).
12. Alexandrovski, A., Fejer, M., Markosian, A. & Route, R. Photothermal common-path interferometry (pci): new developments. *Proc. SPIE, Vol. 7193, id. 71930D* (2009). **7193**, 71930D, DOI: [10.1117/12.814813](https://doi.org/10.1117/12.814813) (2009).
13. Chipman, R. A., Lam, W.-S. T. & Young, G. *Polarized light and optical systems* (CRC press, 2018).

14. Zeidler, S. Numerical tool for calculating birefringence in mirror-substrates for gravitational-wave detectors. *Front. Astron. Space Sci.* **submitted**.
15. Harris, D. C. *et al.* Refractive index of infrared-transparent polycrystalline alumina. *Opt. Eng.* **56**, 077103 (2017).
16. Hearn, E. J. Experimental stress analysis. In *Mechanics of Materials 2*, chap. 6 (Butterworth Heinemann, 1999), 3 edn.
17. Iwaki, T. & Koizumi, T. Stress-optic law in a single crystal and its application to photo-anisotropic elasticity. *Exp. Mech.* **29**, 295–299, DOI: [10.1007/BF02321411](https://doi.org/10.1007/BF02321411) (1989).
18. Nye, J. F. *Physical properties of crystals: their representation by tensors and matrices* (Oxford university press, 1985).
19. Bradley, D. L. *PHOTOELASTIC CONSTANTS OF SYNTHETIC SAPPHIRE*. Master's thesis, Michigan State University (1963).
20. Bruni, F. J. Crystal growth of sapphire for substrates for high-brightness, light emitting diodes. *Cryst. Res. Technol.* **50**, 133–142, DOI: [10.1002/crat.201400230](https://doi.org/10.1002/crat.201400230) (2015).
21. Hirose, E. *et al.* Sapphire mirror for the kagra gravitational wave detector. *Phys. Rev. D* **89**, 062003 (2014).
22. Burns, R. G. *Mineralogical Applications of Crystal Field Theory, 2nd ed.* (Cambridge University Press, Cambridge, 1993).
23. Zeidler, S., Posch, T., Mutschke, H., Richter, H. & Wehrhan, O. Near-infrared absorption properties of oxygen-rich stardust analogs - the influence of coloring metal ions. *Astron. & Astrophys.* **526**, –681 (2011).
24. Ghamnia, E., Jardin, C. & Bouslama, M. Luminescent centres f and f+ in α -alumina detected by cathodoluminescence technique. *J. Electron Spectrosc.* **133**, 55–63, DOI: [10.1016/j.elspec.2003.08.003](https://doi.org/10.1016/j.elspec.2003.08.003) (2003).
25. Barish, B. *et al.* Development of large size sapphire crystals for laser interferometer gravitational-wave observatory. *IEEE TRANSACTIONS ON NUCLEAR SCIENCE* **49**, 1233–1237, DOI: [10.1109/TNS.2002.1039643](https://doi.org/10.1109/TNS.2002.1039643) (2002).

Acknowledgements (not compulsory)

This work was supported by MEXT, JSPS Leading-edge Research Infrastructure Program, JSPS Grant-in-Aid for Specially Promoted Research 26000005, JSPS Grant-in-Aid for Scientific Research on Innovative Areas 2905: JP17H06358, JP17H06361 and JP17H06364, JSPS Core-to-Core Program A. Advanced Research Networks, JSPS Grant-in-Aid for Scientific Research (S) 17H06133, JSPS Grant-in-Aid for JSPS Fellows 20F20803, the joint research program of the Institute for Cosmic Ray Research, University of Tokyo National Research Foundation (NRF) and Computing Infrastructure Project of KISTI-GSDC in Korea, Academia Sinica (AS), AS Grid Center (ASGC) and the Ministry of Science and Technology (MoST) in Taiwan under grants including AS-CDA-105-M06.